Low Dark Current and High Responsivity 1020nm InGaAs/GaAs Nano-Ridge Waveguide Photodetector Monolithically Integrated on a 300-mm Si Wafer

Cenk Ibrahim Ozdemir, *Member, IEEE*, Yannick De Koninck, Didit Yudistira, Nadezda Kuznetsova, Marina Baryshnikova, Dries Van Thourhout, *Member, IEEE*, Bernardette Kunert, Marianna Pantouvaki, *Member, IEEE*, and Joris Van Campenhout, *Member, IEEE*

(Top-Scored Paper)

***Abstract*—We report on high-quality InGaAs/GaAs multi-quantum well waveguide photodetectors, monolithically integrated through metalorganic vapor-phase selective-area epitaxial growth and contact metallization in a 300-mm CMOS pilot line. The photodetectors are implemented using the nano-ridge engineering concept, leveraging aspect-ratio trapping in combination with precise control of the nano-ridge cross section dimensions and composition. The InGaAs/GaAs p-i-n nano-ridge photodetectors are shown to achieve high internal responsivities of up to 0.65 A/W at −1 V bias and 1020 nm wavelength. A clear correlation is observed between measured responsivity and contact-plug design, correlating well with simulation models. In addition, a record-low dark current density of 1.98×10^{-8}A/cm^2 and low absolute dark currents of $<$1 pA are demonstrated, illustrating the high quality of the III-V materials and effective in-situ InGaP surface passivation layers. Initial RF measurements suggest RC-limited photodetection bandwidths in the GHz range. These results illustrate the strong potential of the III-V/Si nano-ridge epitaxy and waveguide device concept, to complement the Silicon Photonics toolbox with high-quality, high-throughput III-V functionality.**

***Index Terms*—III-V semiconductor materials, monolithic integration, nano-ridge engineering, optical simulation, photodetectors, quantum well devices, semiconductor waveguides, silicon photonics.**

Manuscript received March 29, 2021; revised May 21, 2021; accepted May 25, 2021. Date of publication May 27, 2021; date of current version August 30, 2021. This work was funded by IMEC's industry-affiliation Optical I/O R&D Program. *(Corresponding author: Cenk Ibrahim Ozdemir.)*

Cenk Ibrahim Ozdemir and Dries Van Thourhout are with 3D and Silicon Photonics Technologies Department, imec, Kapeldreef 75 3001 Leuven, Belgium, and also with Photonics Research Group, INTEC, Ghent University, C.I.O and D.V.T, Technologiepark-Zwijnaarde 126 9052 Ghent, Belgium (e-mail: cenk.ozdemir@imec.be; dries.vanthourhout@ugent.be).

Yannick De Koninck, Didit Yudistira, Marina Baryshnikova, Bernardette Kunert, Marianna Pantouvaki, and Joris Van Campenhout are with 3D and Silicon Photonics Technologies Department, imec, Kapeldreef 75 3001 Leuven, Belgium (e-mail: yannick.dekoninck@imec.be; didit.yudistira@imec.be; marina.baryshnikova@imec.be; bernardette.kunert@imec.be; marianna.pantouvaki@imec.be; joris.vancampenhout@imec.be).

Nadezda Kuznetsova is with 3D and Silicon Photonics Technologies Department, imec, Kapeldreef 75 3001 Leuven, Belgium and is now with the Micro- Nano Systems, 3001 KU Leuven, Belgium (e-mail: nadezda.kuznetsova@kuleuven.be).

Color versions of one or more figures in this article are available at https://doi.org/10.1109/JLT.2021.3084324.

Digital Object Identifier 10.1109/JLT.2021.3084324

I. Introduction

SILICON photonics (SiPho) has become centerpiece in optical communications and other applications as it enables dense and high throughput integration of photonic devices at low cost and large volume. However, silicon is intrinsically limited by its indirect bandgap and cannot offer all active device capabilities in communications applications. Capabilities such as amplification and detection are typically achieved by introducing additional materials, such as Ge or III-V compound semiconductors. For photodetection, epitaxially grown Ge-on-Si photodetectors offer high responsivity in the O-band and C-band, high bandwidth and acceptable dark current [1]. However, due to its indirect bandgap, Ge does not enable efficient light generation and amplification.

III-V functions can be integrated on Si with a variety of methods: flip-chip bonding of pre-fabricated devices [2], heterogenous integration of externally grown III-V layers through die-to-wafer bonding [3], [4], or heteroepitaxy of III-V layers on Si, either as blanket layers [5], [6], [7], [8], [9], [10], [11], or through selective-area epitaxial growth [12], [13], [14]. Out of these integration methods, monolithic integration based on selective-area growth arguably has the strongest potential for enabling the highest integration throughput and the lowest cost. However, significant mismatches in crystal lattice constants, thermal expansion coefficients and crystal polarities between the Si and epitaxial III-V layers typically result in a variety of crystal defects such as misfit dislocations, threading dislocations, stacking faults and point defects [15]. In blanket epitaxial growth approaches, buffer layers of several micrometers thickness are typically required to accommodate such defects. Alternatively, aspect-ratio trapping (ART) can help to substantially reduce the required buffer layer thickness, by initiating the III-V epitaxial growth in nano-trenches [15]. Above the nano-trenches, the growth of III-V layers with low defect density can be continued to form a nano-ridge (NR) structure, with a volume, shape and composition specifically engineered for the target application, in a flexible epitaxy concept referred to as nano-ridge engineering [16], [17]. In the context of SiPho, NR engineering enables the integration of active III-V waveguides with precisely controlled cross sections and material composition. In addition,

such III-V NR waveguides have the potential for evanescent optical coupling to an underlying Si waveguide [18], leveraging ultra-thin buffer layers enabled by the ART. The NR engineering approach has therefore the potential to realize a fully integrated SiPho platform with monolithic III-V light sources, electrooptic III-V modulators and III-V photodetectors (PDs). Recently, we reported the first proof-of-concept NR waveguide devices, using InGaAs/GaAs multi-quantum well nano-ridge waveguide structures operating around 1020 nm wavelength. In [19], [20], we demonstrated optically pumped lasing. In [21], we reported InGaAs/GaAs multi-quantum well (MQW) nano-ridge waveguide photodetectors (NRWPD) monolithically grown on a 300-mm Si substrate for the first time, exhibiting 10 pA dark current, and 0.25A/W internal responsivity at -1 V bias, for the wavelength of 1020 nm. In addition, the NR concept has recently been extended to ternary InGaAs devices [17], enabling operating wavelengths beyond 1200 nm, and providing a better fit for integration in SiPho platforms.

In this paper, along with our earlier demonstration in [22], we demonstrate InGaAs/GaAs MQW NRWPDs with strongly improved internal responsivities up to 0.65A/W, or 79% internal quantum efficiency. In addition, the devices show a remarkably low dark current of just $\sim$0.05 pA at -2 V bias voltage. This is almost three orders of magnitude lower than previously reported [21], and to the best of our knowledge the lowest dark current ever reported for a monolithic III-V on Si photodetector [3]–[12]. In comparison with [21], the single step epitaxial growth and reduced contact plug densities improved the device performances. In addition, we report a detailed study of the impact of contact plug design parameters and device length on the NRWPD responsivity, supported by optical simulations. Finally, initial radio-frequency (RF) S11-parameter measurements are reported, suggesting that the reported devices are capable of photodetection with bandwidth in the GHz range, limited by the RC time constant in these early devices.

II. Device Design and Fabrication

The NRWPD devices were fully patterned on a Si (001) substrate in imec's 300-mm CMOS pilot line. The device fabrication started with a blanket ion implant step, targeting n-type doping with 1×10^{19} cm^{-3} peak concentration. Next, Si stripes with 100 nm nominal width and 300 nm depth were patterned using a shallow-trench isolation (STI) module. After the oxide planarization, a Si wet-etch step was carried out to from the nano-trenches using tetramethylammonium hydroxide (TMAH), resulted a V-shaped trench bottom with exposed {111} facets of Si for suppressing the anti-phase domain formation at the GaAs/Si interface during the subsequent epitaxial growth. Next, the III-V metalorganic vapor-phase epitaxy (MOVPE) started with the growth of an n-type doped GaAs layer on these {111} Si facets, filling the nano trenches. Misfit defects initiated at the GaAs/Si interface were effectively confined inside the trenches [15]. The subsequent GaAs layer, grown out of the trenches, has a misfit defect density below 1×10^6 cm^{-2} [16], and served as a fully relaxed buffer for the growth of active layers on the top. The active region of three $In_{0.22}Ga_{0.78}As$ QWs with a targeted thickness of 10 nm, embedded in a non-intentionally-doped (intrinsic) i-GaAs layer. A p-i-n diode was formed in the NR structure by introducing dopants during the epitaxial growth of the bottom and the top GaAs layers. The target doping concentrations were about 1×10^{19} cm^{-3} for n-type and p-type GaAs layers. Finally, the InGaAs/GaAs NR was capped with a lattice-matched, conformal InGaP layer to passivate the GaAs surfaces. By carefully optimizing the epitaxial growth parameters throughout the process, as using the NR engineering principles, rectangular waveguide shapes of the nano-ridges were achieved on top of the nano-trenches, with a final nano-ridge waveguide height of 470 nm and a width of 505 nm. After oxide filling and planarization, the InGaP layer was locally etched and tungsten contact plugs were formed to electrically contact the top p-GaAs layer. The bottom n-GaAs layer was connected through the n-doped Si substrate to another set of tungsten contact plugs. The fabrication was completed using standard CMOS Cu damascene metallization processing. A schematic cross-section and a cross-section scanning-electron microscopy (XSEM) image of the final structure are shown in Fig. 1.

TABLE I
Reported Device Sites

Design Parameter	Unit	**Site A**	**Site B**
Length	μm	500	5, 20, 45, 95, 120
Plug pitch	μm	0.6, 1.2, 2.4, 4.8	0.3, 0.6, 1.5

After the fabrication, photoluminescence (PL) measurements were carried out, revealing a peak emission wavelength at 1040 nm and band-edge at 1110 nm, confirming the target indium composition of 22% and thickness of the InGaAs/GaAs MQW stack (Fig. 1 bottom).

The target dimensions and composition of the NRWPD devices were chosen to realize a strong overlap between the optical guide mode supported by the NR waveguide and the active region, resulting in a strong optical absorption of the guide mode in the InGaAs MQW stack. From the optical mode simulation (using Lumerical MODE), the optical confinement factor in the MQW layers was derived to be $\Gamma_{\mathrm{QW}} \cong 8.2\%$. In addition, the doping profile was determined to achieve a sufficiently strong electrical field across the same active region under reverse bias, to realize efficient collection of the photogenerated carriers. The electric field in the volume of the intrinsic GaAs region comprising the InGaAs QWs was calculated (using TCAD Sentaurus Device) to be more than 50 kV/cm at -1 V bias. As such, the design shows strong potential as an efficient photodetector.

III. Static Electrooptic Performance

After the wafer-scale processing, two sets of samples were prepared by cleaving dies to form optical facets for optical edge coupling. Devices were prepared from two distinct sites A and B, which contain designs with p-contact plugs on different pitch distances along the waveguide, as well as different device lengths, as described in Table I. Site A gave access to NRWPD devices of up to 500 μm length. The pitch of the p-contacts to the

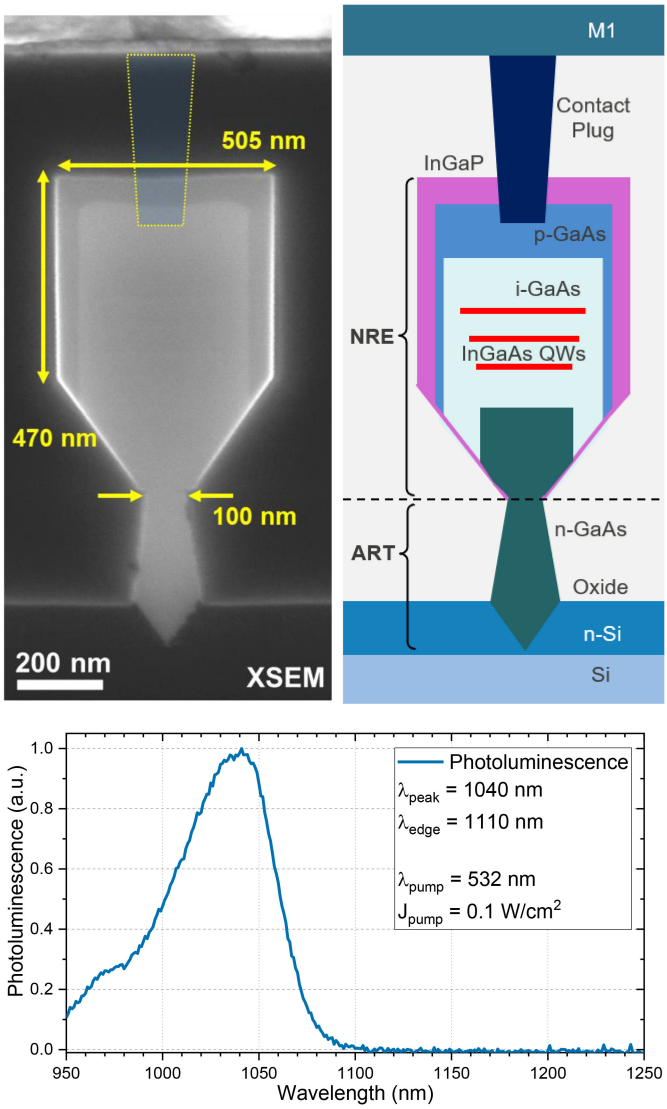

Fig. 1. *(top left)* Cross-section scanning electron microcopy (XSEM) image of a GaAs nanoridge with three InGaAs QWs. *(top right)* Schematic description of nano-ridge cross-section. *(bottom)* Photoluminescence of the quantum wells, pumped with 532 nm 15 kHz pulsed laser with 0.1 W/cm^2 intensity.

p-GaAs layer was varied from 0.6 μm, to 1.2 μm, 2.4 μm, and 4.8 μm in site A. Site B contained NRWPD device lengths from 5 μm to 120 μm, with p-contact pitch values of 0.3 μm, 0.6 μm and 1.5 μm. The actual length of measured devices depended on the precision of the cleaving position, which had a variability of about $\pm$4 μm.

The first electrical characterization of devices from site A reveals p-i-n diode behavior with more than 6 orders of magnitude rectification (Fig. 4(a)). Measured forward-bias dark currents depend on p-contact plug pitch due to variance in contact resistivity. The 500 μm long devices in site A exhibited a very low dark current of median 0.05 pA at -2 V (Fig. 4(c)). Median dark current at -1 V was observed around the noise floor of the of the measuring tool (Keysight B1500A Semiconductor Device Analyzer) at 5 fA. No clear dependence is observed between the contact plug pitch and reverse dark current. Taking into account

TABLE II
BENCHMARK OF DARK CURRENTS OF PHOTODETECTORS MONOLITHICALLY INTEGRATED ON SI

Reference	Material	V (V)	λ (nm)	BW (GHz)	R (A/W)	J_{dark} (A/cm^2)
[1]	Ge	-1	1310	67	0.93	3.4×10^{-2}
[3]	III-V	-4	N\A	32	0.15	0.1×10^{0}
[4]	III-V	-4	1260	65	0.5	3.3×10^{-2}
[5]	III-V	-1	1250	2.3	0.9	0.8×10^{-4}
[6]	III-V	-3	1310	5.5	0.08	1.3×10^{-4}
[7]	III-V	-3	1550	9	0.79	8.0×10^{-4}
[8]	III-V	-1	1300	N\A	0.26	3.5×10^{-7}
[9]	III-V	-5	1310	2.3	0.234	6.6×10^{-5}
[10]	III-V	-3	1550	28	0.27	1.0×10^{-1}
[11]	III-V	-2	850	N\A	0.17	4.5×10^{-7}
[23]	III-V	-1.5	1346	25	0.4	1.4×10^{0}
[13]	III-V	-2	1346	25	0.68	2.8×10^{0}
[14]	III-V	-0.5	1550	N\A	1.06	3.3×10^{-2}
[21]	III-V	-1	1020	N\A	0.25	1.4×10^{-5}
[22], This work	III-V	-2	1020	1.9*	0.68	**1.9×10^{-8}**

the 505 nm width (as measured on SEM images) and 500 μm length of the NRs in site A, this corresponds to an equivalent dark current density of 1.98×10^{-8} A/cm^2 at -2 V, which is the lowest reported dark current for III-V photodetectors monolithically grown on Si [3]–[12]. In Table II, a comparison is shown for the dark current densities and the responsivities measured for the photodetectors monolithically grown on Si, using different material stacks. In this benchmarking, it is important to note that the device reported here have a higher bandgap compared to many of other reported devices.

Next, the InGaAs/GaAs NRWPDs were characterized electro-optically by coupling a 1020 nm wavelength laser through the cleaved facets of the devices using a HI-1060 metal tapered lensed fiber with 2.0 μm mode field diameter (MFD) (Fig. 3). The output power at the tip of the lensed fiber was measured to be $+7.00$ dBm ($+/-1\%$) (5.01 mW $+/-0.06$ mW). This power level was set as the nominal level in further experiments. The fiber was actively aligned using the photocurrent read-out from the device.

The current-voltage (I-V) measurements with light injection were 8 to 10 orders of magnitude higher than the measured dark currents, as shown in Fig. 4(a). The measured light currents at reverse bias are observed to be higher than those at forward bias, which may be related to less efficient carrier collection.

After subtracting the measured dark current, the extracted photocurrents are in the range 100–800 μA (Fig. 4(b)) and show a clear dependency on the contact plug pitch. As shown in Fig. 2, the top contact plugs are in close proximity to the optical mode of the NRWPD, and are expected to contribute strongly to the optical losses of the waveguide mode, as being discussed in more detail in the next section. The fiber-referred responsivities, the ratio of photocurrent to the measured fiber-tip power, correlate strongly with the plug pitch parameter. For the shortest contact pitch of 0.3 μm, the median fiber-referred responsivity of the

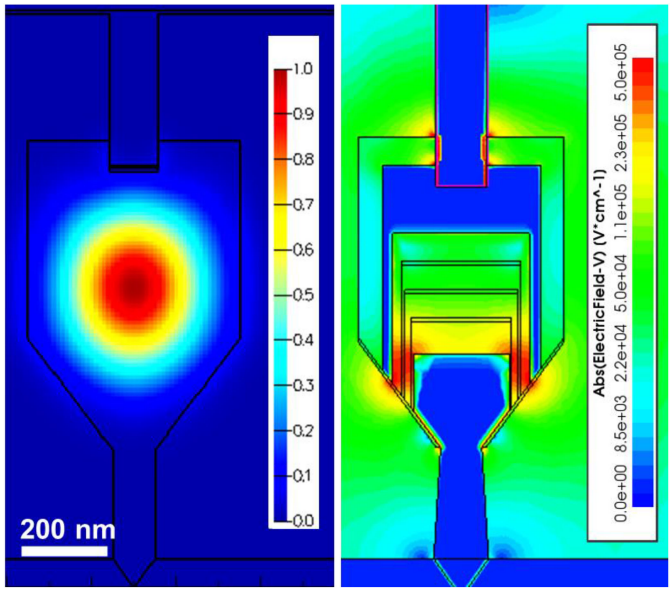

Fig. 2. *(left)* $|E|^2$ profile of fundamental TE mode supported in NRWPD, in arbitrary units, calculated with Lumerical Mode. For the fundamental TE mode, QWs' confinement factor is found as $\Gamma_{QW} \cong 8.2\%$. *(right)* Absolute E-field profile at -1 V bias calculated with Sentaurus Device, arcsinh color-scaled in the range of $0 - 5 \times 10^5$ V/cm.

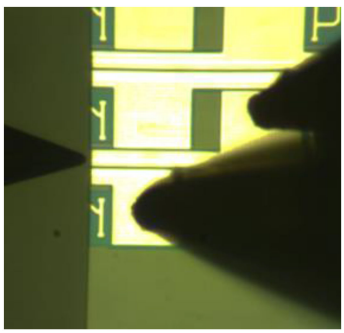

Fig. 3. Top view of measurement setup with the facet and the lensed fiber.

NRWPDs is ~0.03 A/W for 1020 nm wavelength at -1 V bias. It increases to ~0.14 A/W for 4.8 μm plug pitch.

Power dependent measurements are carried out at reduced input power levels from the nominal level, for the devices in site B with lengths larger than calculated absorption lengths. In the plot of photocurrent vs. fiber-tip power, the resulting points linearly fit based on their bias voltage and contact plug pitch, as shown in Fig. 5, and gives no sign of saturation.

IV. Responsivity Analysis and Simulations

The mode field diameter (MFD) of the fundamental TE mode of the NRWPD device was calculated to be 0.42 μm ($1/e^2$), as shown in Fig. 2. In comparison with the 2 μm MFD of the focused beam of the lensed fiber, this reveals a significant mode size mismatch leading to relatively low fiber-to-NRWPD coupling efficiencies in the edge coupling configuration. In order to

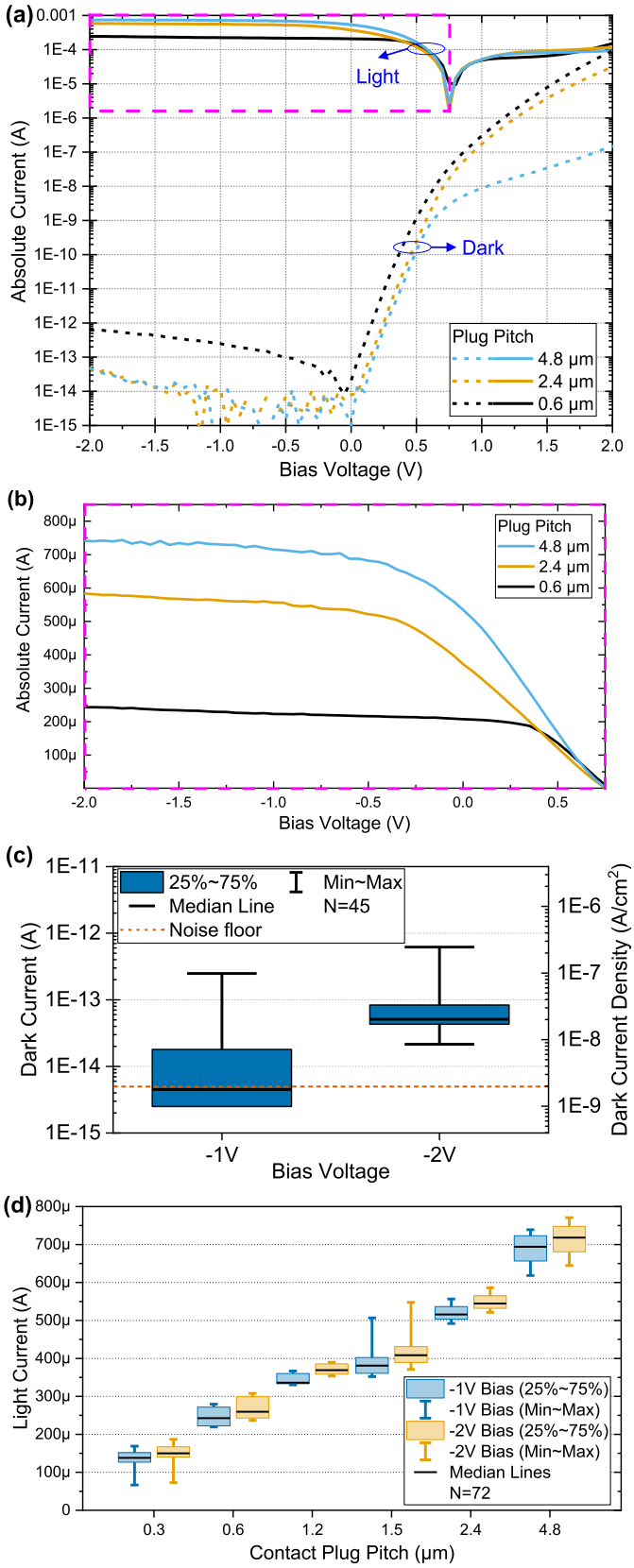

Fig. 4. (a) Dark (dash) and light (line) I-V curves of devices with different p-contact plug pitches in site A. (b) Light I-V zoom in at linear scale. (c) Dark current statistics at different bias voltages for all devices. (d) Light current statistics of devices with different p-contact plug pitches at different bias voltages, measured at nominal input power.

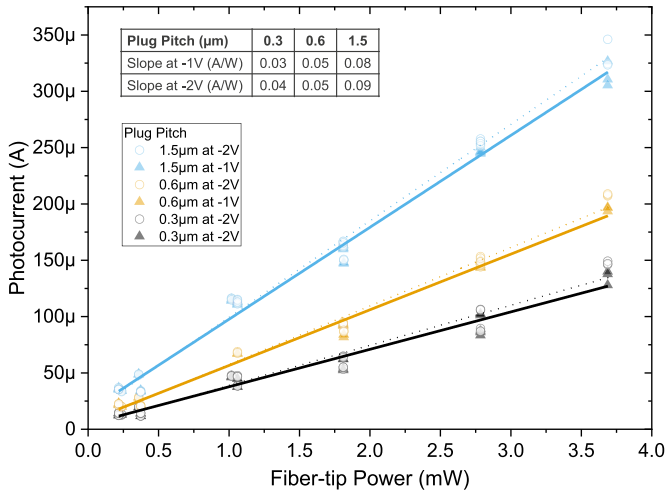

Fig. 5. Photocurrent vs. fiber-referred power of the devices in site B that are longer than the absorption length. Grouped and linearly fitted with respect to bias voltage and contact plug pitch. *(inset)* Table of linear fitting slopes for each case.

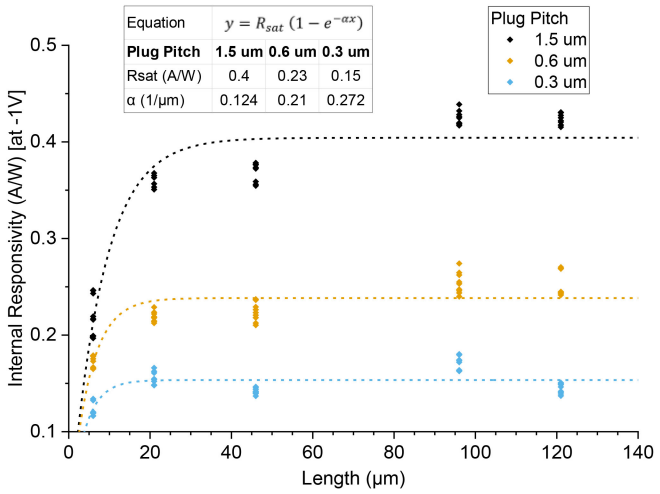

Fig. 6. Internal responsivity vs length at -1 V of the devices measured at nominal input power in site B. Data points are grouped with respect to contact plug pitch. Fitting is based on an exponential saturation formula based on Beer-Lambert Law. Both absorption coefficients and saturation responsivities are observed to be dependent on the contact plug pitch. *(inset)* Table with the fitting equation and the extracted parameters of R_{sat} and α absorption coefficient.

evaluate the internal photodetector responsivity, the coupling efficiency $\eta_{coupling}$ from the lensed fiber into the NRWPD was estimated using finite-difference time domain (FDTD) simulations in 3-dimensions (using Lumerical software). The total coupling efficiency from the TE-polarized 2.0 μm MFD Gaussian beam of the lensed fiber into the nano-ridge waveguide was found to be 21%, considering only the 10 lowest-order modes, with the majority of the light (86%) coupling into the fundamental TE mode. The coupled power (P_c), internal responsivity (R_{int}) and internal quantum efficiency (η_{int}) are then calculated with the following formulas:

$$P_c = P_{out,lensed\ fiber} \times \eta_c \tag{1}$$

$$R_{int} = (I_{light} - I_{dark})/P_c \tag{2}$$

$$\eta_{int} = R_{int}\hbar\omega/e \tag{3}$$

where $\hbar$ is the reduced Planck constant, ω is frequency and e is electron charge. Based on formulas (2) and (3), the internal responsivities and corresponding internal quantum efficiencies are calculated for both device sites A and B, at -1 V and at -2 V biases.

Responsivities of short length devices can be written with an exponential saturation formula based on Beer-Lambert law as:

$$R\ (x\,[um]) = R_{sat}\ \left(1 - e^{-\alpha x}\right) \tag{4}$$

where R_{sat} is the saturation responsivity, α (1/μm) is the total absorption coefficient. The total absorption coefficient can be separated as:

$$\alpha\ = \alpha_{MQW}\ + \alpha_{metal} + \alpha_{FCA} \tag{5}$$

where α_{MQW}, α_{metal}, α_{FCA} are MQW, metal and free carrier absorption coefficients, respectively. Measured internal responsivities of the short length devices in site B at -1 V are fitted with this equation (Fig. 6). The fitted results reveal the contact plug pitch dependence of both maximum responsivity (R_{sat} of the fitting) and extracted total absorption coefficient α. Based on the fitted α values for different plug densities, an absorption coefficient of 0.088 1/μm is found for the nano-ridges without p-contact plugs ($\alpha_{MQW} + \alpha_{FCA}$). This is in good agreement with the MQW modal absorption of 0.072 1/μm of fundamental TE mode, calculated in optical mode simulations, only for α_{MQW}. The absorption coefficient of 0.088 1/μm gives the 99% absorption length as 53 μm. Beyond this length, all the input light assumed to be absorbed. This absorption length gets shorter for higher plug densities due to metal losses.

Devices longer than the absorption length in site A and B were further characterized at the nominal input power level at 1020 nm for their internal responsivities. Aggregated data is shown in Fig. 7, grouped with respect to the p-contact plug pitch. The highest responsivities were found on the devices with 4.8 μm p-contact plug pitch. The median internal responsivities (internal quantum efficiencies) of 4.8 μm plug pitch devices were calculated to be 0.65 A/W (79%) at -1 V and 0.68 A/W (82%) at -2 V bias at 1020 nm laser wavelength (Fig. 7).

A second set of 3D FDTD simulations was completed to further investigate the effect of the p-contact plug pitch on transmission loss. This considered a uniform GaAs waveguide with no lossy material except the p-contact plugs. 3D nano-ridges with different p-contact plug pitches were excited with the fundamental TE-mode and the transmission is calculated after a 4.8 μm distance as shown in Fig. 8. The calculated transmission values are reported in Fig. 7(grey lines). The internal responsivity levels follow this p-contact plug pitch dependence, suggesting that the drop in the internal responsivities for smaller contact pitch values is linked to the loss induced by the optical absorption at the metal contacts. This result helps us also differentiating the responsivity reducing mechanisms of the NRWPD devices and can help further improve the device performance in future.

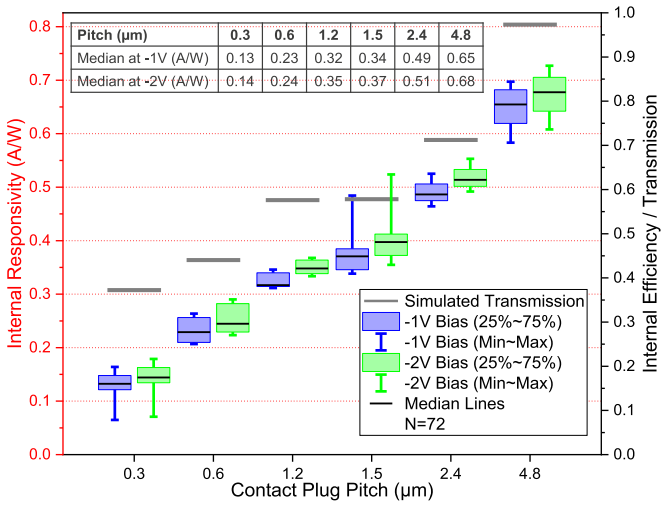

Fig. 7. Responsivity distributions for different biases and p-contact plug pitches of devices from both sites A and B excited with nominal input power. Site B data excluded devices shorter than the corresponding absorption lengths. *(grey bars)* Simulated transmission values for different p-contact plug pitches, scaled to right vertical axis. *(inset)* Table of median responsivity values.

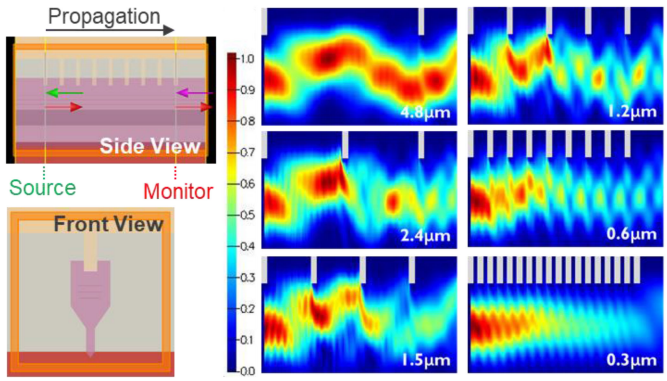

Fig. 8. 3D FDTD simulations for calculating p-contact plug effects. *(left)* Side and front view of constructed simulation structure in Lumerical FDTD. *(right)* Side view of 2D power distribution at center for different p-contact plug pitches, grey plug shapes externally added for clarity.

V. Device Capacitance and Resistance

The dynamic response of p-i-n photodetectors is typically limited both by the RC constant and the carrier transit time. In the case of the NRWPD, simulations suggest that carriers generated in the InGaAs MQW region will experience electric fields of ~50 kV/cm and attain drift velocities of 0.8×10^7 cm/s [24] and 1.0×10^7 cm/s [25], for electrons and holes respectively. Considering transit lengths smaller than 200 nm in the intrinsic region of the NRWPD, the carrier transit time related bandwidth exceeds 400 GHz and is not expected to be a limiting factor.

To assess the RC bandwidth, the S_{11} response of the NRWPD devices was measured using a 50 GHz vector network analyzer in a 1-port configuration. These measurements were carried out on a non-cleaved device where RF pad configurations with and without NRWPD devices were available. This helps to de-couple the external pad effects, and accurately extract device series

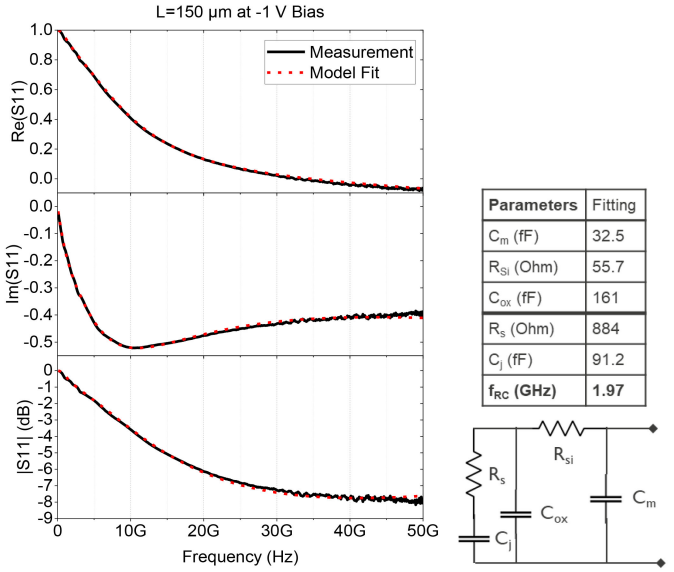

Fig. 9. S11 response of a 150 μm long NRWPD at -1 V bias and fitting based on the simplified equivalent circuit. Metal capacitance (C_m), silicon resistance (R_{Si}) and oxide capacitance (C_{ox}) parameters are extracted from reference pad with same contact pad design but without NRWPD device. With those parameters, model fitting on the NRWPD's S11 response (R-square of 0.996) results in a series resistance (R_s) and junction capacitance (C_j).

resistance (R_s) and junction capacitance (C_j). For a NRWPD device with 0.3 μm contact plug pitch and 150 μm length at -1 V bias we find $C_j = 91$ fF and $R_s = 884$ Ohm, suggesting an intrinsic RC-limited opto-electrical bandwidth of 1.9 GHz. Based on a ~23 kOhm ($\pm$10%) contact resistance per plug obtained from transfer length method measurements, this extrapolates to 1.1 GHz for the 4.8 μm contact plug pitch case. We believe there is a strong potential exists for higher bandwidths in future NRWPD devices. In future devices, the junction capacitance can be reduced by carefully optimizing the device cross section and eliminating the p-doped GaAs sidewalls, and the series resistance can be reduced by optimizing the contacting and the p-type doping profile.

VI. Conclusion

We reported high-quality InGaAs/GaAs MQW p-i-n nano-ridge waveguide photodetectors, monolithically integrated in a 300-mm Si pilot line through selective-area epitaxial growth with aspect-ratio trapping and nano-ridge engineering. At 1020 nm wavelength, the photodetectors with the lowest contact density exhibit an internal responsivity of 0.65 A/W, or 79% internal quantum efficiency. A detailed analysis of the responsivity dependence on device length and metal contact pitch is reported, as well as a good correlation with simulation models.

In addition, a record-low dark current density of 1.98×10^{-8} A/cm^2 is reported at -1 V bias, illustrating the high material quality of the InGaAs/GaAs structures as well as the effective InGaP passivation. Finally, initial RF measurements and electric-field simulations suggest that the bandwidth in current devices is predominantly limited by the RC constant, and estimated to be 1.1–1.9 GHz. In summary, this work illustrates

the potential of the III-V nano-ridge epitaxy concept to integrate high-quality III-V waveguide devices directly on Si.

ACKNOWLEDGEMENT

This work was realized by imec's industry-affiliation Optical I/O R&D Program.

REFERENCES

[1] H. Chen *et al.*, "−1 v bias 67 GHz bandwidth Si-contacted germanium waveguide p-i-n photodetector for optical links at 56 gbps and beyond," *Opt. Exp.*, vol. 24, no. 5, p. 4622, pp. 4622–4631, Mar. 2016.

[2] J. Zhang *et al.*, "Silicon photonics fiber-to-the-home transceiver array based on transfer-printing-based integration of III-V photodetectors," *Opt. Exp.*, vol. 25, no. 13, Jun. 2017, Art. no. 14290.

[3] Y. Baumgartner *et al.*, "Novel CMOS-compatible ultralow capacitance hybrid ili-V/Si photodetectors tested up to 32 gbps NRZ," in *Proc. Opt. Fiber Commun. Conf. Exhib.*, Mar. 2019, pp. 1–3.

[4] Y. Baumgartner *et al.*, "High-speed CMOS-compatible III-V on si membrane photodetectors," *Opt. Exp.*, vol. 29, no. 1, Jan. 2021, Art. no. 509.

[5] Y. Wan *et al.*, "Monolithically integrated InAs/InGaAs quantum dot photodetectors on silicon substrates," *Opt. Exp.*, vol. 25, no. 22, Oct. 2017, Art. no. 27715.

[6] D. Inoue *et al.*, "Low-dark current 10 Gbit/s operation of InAs/InGaAs quantum dot p-i-n photodiode grown on on-axis (001) GaP/Si," *Appl. Phys. Lett.*, vol. 113, no. 9, Aug. 2018, Art. no. 093506.

[7] K. Sun *et al.*, "Low dark current III–V on silicon photodiodes by heteroepitaxy," *Opt. Exp.*, vol. 26, no. 10, May 2018, Art. no. 13605.

[8] J. Huang *et al.*, "Defect characterization of InAs/InGaAs quantum dot p-i-n photodetector grown on gaAs-on-V-grooved-Si substrate," *ACS Photon.*, vol. 6, no. 5, pp. 1100–1105, May 2019.

[9] B. Chen *et al.*, "Low dark current high gain InAs quantum dot avalanche photodiodes monolithically grown on si," *ACS Photon.*, vol. 7, no. 2, pp. 528–533, Feb. 2020.

[10] K. Sun, J. Gao, D. Jung, J. Bowers, and A. Beling, "40 Gbit/s waveguide photodiode using III–V on silicon heteroepitaxy," *Opt. Lett.*, vol. 45, no. 11, Jun. 2020, Art. no. 2954.

[11] H. Mehdi *et al.*, "Monolithic integration of GaAs p–i–n photodetectors grown on 300 mm silicon wafers," *AIP Adv.*, vol. 10, no. 12, Dec. 2020, Art. no. 125204.

[12] S. Mauthe *et al.*, "Ultra-thin III-V photodetectors epitaxially integrated on si with bandwidth exceeding 25 GHz," in *Proc. Opt. Fiber Commun. Conf.*, 2020, Art. no. M3D.3.

[13] S. Mauthe *et al.*, "High-speed III-V nanowire photodetector monolithically integrated on si," *Nat. Commun.*, vol. 11, no. 1, Dec. 2020, Art. no. 4565.

[14] Y. Xue, Y. Han, Y. Wang, Z. Zhang, H. K. Tsang, and K. M. Lau, "Bufferless III–V photodetectors directly grown on (001) silicon-on-insulators," *Opt. Lett.*, vol. 45, no. 7, Apr. 2020, Art. no. 1754.

[15] B. Kunert, Y. Mols, M. Baryshniskova, N. Waldron, A. Schulze, and R. Langer, "How to control defect formation in monolithic III/V heteroepitaxy on (100) si? A critical review on current approaches," *Semicond. Sci. Technol.*, vol. 33, no. 9, Sep. 2018, Art. no. 093002.

[16] M. Baryshnikova *et al.*, "Nano-ridge engineering of GaSb for the integration of InAs-GaSb heterostructures on 300 mm (001) si," *Crystals*, vol. 10, no. 4, Apr. 2020, Art. no. 330.

[17] B. Kunert *et al.*, "Application of an sb surfactant in InGaAs nano-ridge engineering on 300 mm silicon substrates," *Cryst. Growth Des.*, vol. 21, no. 3, pp. 1657–1665, Mar. 2021.

[18] Y. Shi, B. Kunert, Y. De Koninck, M. Pantouvaki, J. Van Campenhout, and D. Van Thourhout, "Novel adiabatic coupler for III-V nano-ridge laser grown on a si photonics platform," *Opt. Exp.*, vol. 27, no. 26, Dec. 2019, Art. no. 37781.

[19] Y. Shi *et al.*, "Optical pumped InGaAs/GaAs nano-ridge laser epitaxially grown on a standard 300-mm si wafer," *Optica*, vol. 4, no. 12, Dec. 2017, Art. no. 1468.

[20] D. Van Thourhout *et al.*, "Nano-ridge laser monolithically grown on (001) si," in *Future Directions in Silicon Photonics*. C. Jagadish, S. Lourdudoss, and J. E. Bowers, Eds. Cambridge, MA, USA: Academic Press, 2019, pp. 283–304.

[21] C. I. Ozdemir *et al.*, "InGaAs/GaAs multi-quantum well nano-ridge waveguide photodetector epitaxially grown on a 300-mm si wafer," in *Proc. IEEE Photon. Conf.*, Sep. 2020, pp. 1–2.

[22] C. I. Ozdemir *et al.*, "0.3pA Dark current and 0.65A/W responsivity 1020nm InGaAs/GaAs nano-ridge waveguide photodetector monolithically integrated on a 300-mm si wafer," in *Proc. Eur. Conf. Opt. Commun.*, Dec. 2020, pp. 1–4.

[23] S. Mauthe *et al.*, "Ultra-thin III-V photodetectors epitaxially integrated on si with bandwidth exceeding 25 GHz," in *Proc. Opt. Fiber Commun. Conf.*, 2020, Paper M3D.3.

[24] J. Požela and A. Reklaitis, "Electron transport properties in GaAs at high electric fields," *Solid-State Electron,* vol. 23, no. 9, pp. 927–933, Sep. 1980.

[25] V. L. Dalal, A. B. Dreeben, and A. Triano, "Temperature dependence of hole velocity in p-GaAs," *J. Appl. Phys.*, vol. 42, no. 7, pp. 2864–2867, Jun. 1971.